2015

High Aspect Ratio Carbon Nanotube Membranes Decorated with Pt Nanoparticle Urchins for Micro Underwater Vehicle Propulsion via H2O2 Decomposition

Kevin Marr
Brigham Young University - Provo

Bolin Chen
Iowa State University, cbl0511@iastate.edu

Eric J. Mootz
Iowa State University

Jason Geder
United States Naval Research Laboratory

Marius Pruessner
United States Naval Research Laboratory

See next page for additional authors

Authors
Kevin Marr, Bolin Chen, Eric J. Mootz, Jason Geder, Marius Pruessner, Brian J. Melde, Richard R. Vanfleet, Igor L. Medintz, Brian D. Iverson, and Jonathan C. Claussen

High Aspect Ratio Carbon Nanotube Membranes Decorated with Pt Nanoparticle Urchins for Micro Underwater Vehicle Propulsion *via* H_2O_2 Decomposition

Kevin M. Marr,[†] Bolin Chen,[‡] Eric J. Mootz,[‡] Jason Geder,[§] Marius Pruessner,[§] Brian J. Melde,[§] Richard R. Vanfleet,[∥] Igor. L. Medintz,[§] Brian D. Iverson,*[,†] and Jonathan C. Claussen*[,‡]

[†]Department of Mechanical Engineering, Brigham Young University, 435 Crabtree, Provo, Utah 84602, United States, [‡]Department of Mechanical Engineering, Iowa State University, 2104 Black Engineering, Ames, Iowa 50011, United States, [§]U.S. Naval Research Laboratory, 4555 Overlook Avenue SW, Washington, D.C. 20375, United States, and [∥]Department of Physics and Astronomy, Brigham Young University, N283 Eyring Science Center, Provo, Utah 84602, United States

ABSTRACT The utility of unmanned micro underwater vehicles (MUVs) is paramount for exploring confined spaces, but their spatial agility is often impaired when maneuvers require burst-propulsion. Herein we develop high-aspect ratio (150:1), multiwalled carbon nanotube microarray membranes (CNT-MMs) for propulsive, MUV thrust generation by the decomposition of hydrogen peroxide (H_2O_2). The CNT-MMs are grown *via* chemical vapor deposition with diamond shaped pores (nominal diagonal dimensions of 4.5 × 9.0 μm) and subsequently decorated with urchin-like, platinum (Pt) nanoparticles *via* a facile, electroless, chemical deposition process. The Pt-CNT-MMs display robust, high catalytic ability with an effective activation energy of 26.96 kJ mol^{-1} capable of producing a thrust of 0.209 ± 0.049 N from 50% [w/w] H_2O_2 decomposition within a compact reaction chamber of eight Pt-CNT-MMs in series.

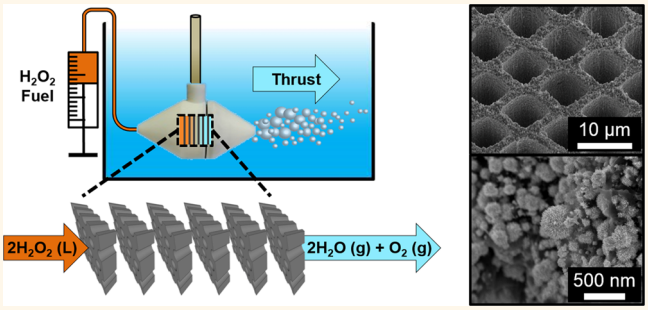

KEYWORDS: underwater propulsion · hydrogen peroxide · carbon nanotube · platinum · nanoparticle · microchannel · thrust

An upward trend in the research and use of unmanned underwater vehicles (UUVs), and in particular micro underwater vehicles (MUVs, small UUVS between 1 and 50 cm in length), for exploration of confined spaces such as ship wrecks, submerged oil pipelines, and various military purposes has been observed over recent years.[1−3] The locomotion of these vehicles is typically controlled by propeller-based systems, which are often used for long-endurance missions.[4−6] However, propeller-based systems are usually limited in their ability to perform tight radius turns, burst-driven docking maneuvers, and low-speed course corrections.[2,7] These motions often require energy-dense fuels, which can be quickly and efficiently utilized to provide sudden bursts of propulsion. Such energy-dense fuels/reagents include hydrogen peroxide (H_2O_2),[8] methanol,[9] and carbohydrates,[10] all of which have been the focus of many recent fuel-catalyst reaction studies.

The decomposition of H_2O_2 as a means for locomotion in microscale applications is of particular interest because of its scalability, as well as possessing a large power density (up to 45 times that of Ni−Cd batteries in MUVs).[11] In addition, H_2O_2 is an environmentally friendly fuel, expending only "green" byproducts (*i.e.*, oxygen, O_2, and water) during decomposition.[7] Specifically, when exposed to a metal catalyst such as platinum (Pt), H_2O_2 is broken down in an exothermic reaction into O_2 (and water), which provides thrust through the significant volumetric change relative to the liquid fuel.

* Address correspondence to bdiverson@byu.edu, jcclauss@iastate.edu.

Received for review April 9, 2015 and accepted June 24, 2015.

Published online June 24, 2015
10.1021/acsnano.5b02124

Many micro/nanoscale structures have been fabricated to utilize the decomposition of H_2O_2 by Pt for propulsion, including janus motors,[12−14] conical-shaped bubble thrusters,[15−18] and catalytic nano/micromotors.[19−21] In other examples, structures resembling a parallel arrangement of microtubular bubble thrusters[22,23] has also been investigated to achieve design requirements of high aspect ratio and small volumetric profile. Each of these structures rely on transport-enhancing mechanisms to decompose H_2O_2 fuel. We likewise propose a catalytic structure that employs transport-enhancement, but that can be fabricated for burst-propulsion of MUVs and their associated payloads. Thrust required for these applications is provided by the fabrication of scalable catalytic structures which offer the high surface area to fuel volume ratios required for burst-propulsion, while maintaining a small volumetric profile.

Carbon nanotube (CNT)-templated microfabrication is a new approach to constructing high aspect ratio structures that capitalizes on the very large length to diameter ratios present for carbon nanotubes.[24,25] For modest growth lengths of 1 mm and a nominal 100 nm spacing between carbon nanotubes, aspect ratios of 10−10 000 are achievable for vertically aligned growth. When combined with lithographically defined growth, almost any aspect ratio in this range can be realized. This range is significantly better than typical etching techniques for high aspect ratio structures such as deep reactive ion etching (DRIE) and offers distinct advantages over lithography, electroplating, and molding (LIGA) in cost, time, and scalability.[24] Using patterned CNTs as a scaffold, additional materials can be coated on or "infiltrated" into the forest, making these structures rigid and reinforced. The conditions and duration of an infiltration procedure can be controlled to result in highly dense or highly porous regions. Therefore, two-tier, porous materials can be constructed with CNT-templated microfabrication: larger (micron-scale) spacings controlled by lithography and smaller (nanometer-scale) spacings controlled by carbon nanotube forest density and subsequent infiltration. Multiwalled carbon nanotube microarray membranes (CNT-MMs) fabricated by this method thereby provide a versatile microstructure for reagent-based burst-propulsion. Thus, this distinct CNT-templated microfabrication process enables the growth of aligned, high aspect ratio CNT microchannel membranes—a three-dimensional microstructure that cannot be formed from conventional, stand-alone CNT fabrication techniques such as screen-printing,[26,27] electropraying,[28] alcohol catalytic chemical vapor deposition,[29] plasma-enhanced chemical vapor deposition,[30−32] self-assembled monolayer linking,[33] and thermal cross-linking.[34]

Electroless deposition of Pt onto CNTs has been demonstrated in the literature; CNT-MM structures can be functionalized in like manner to provide highly catalytic microstructures for burst-propulsion applications. For example, deposition by the reduction of chloroplatinic acid is a simple, one-step process offering several advantages as shown by Sun *et al.*[35−37] Most notably is that the morphology and density of Pt nanoparticles on carbon structures is controllable. Similar depositions performed on highly ordered 3D graphene by Wang *et al.* demonstrated that this technique provides effective electrocatalytic functionalization for scalable substructures.[38] Furthermore, we have previously demonstrated that Pt deposited in this fashion on nanocellulose is highly durable during MUV propulsion tests using 30% [w/w] H_2O_2.[7] On this basis, we hypothesize that electroless deposition of Pt nanoparticles by the reduction of chloroplatinic acid will provide a controllable, scalable, and mechanically robust[39] catalytic structure for the aggressive decomposition of H_2O_2 fuel at higher concentrations, *i.e.*, 50% [w/w].

Following deposition, Pt-CNT-MMs were inspected and characterized using both scanning electron microscopy (SEM) and transmission electron microscopy (TEM) methods which revealed continuous coverage of Pt on the CNT microchannels. Additional characterization of these structures is reported including hydrophobicity from water contact angle analysis, electroactive specific surface area from cyclic voltammetry (CV) experiments, surface area calculated from Brunauer−Emmett−Teller (BET) analysis on nitrogen adsorption experiments, as well as effective activation energy from H_2O_2 decomposition profiles. Performance of Pt-CNT-MMs in decomposing H_2O_2 was quantified by measuring thrust for a submersible test vehicle. Propulsion testing showed a maximum average thrust of 0.209 ± 0.049 N using eight, inline Pt-CNT-MMs exposed to 50% [w/w] H_2O_2 in a manually driven high burst flow. This generated thrust falls within the milli-Newton thrust range typically required for MUV propulsion,[7,40] while leaving the door open for thrust generation improvement through the inclusion of additional Pt-CNT-MMs in the reaction chamber. This work represents the first-ever reported union of CNT-templated microfabricated structures with electroless chemical deposition of catalytic Pt nanoparticles for thrust generation by the decomposition of H_2O_2 for MUVs.

RESULTS AND DISCUSSION

Design and Fabrication of CNT-MMs. The high-aspect ratio CNT-MMs presented here were fabricated using CNT-templated microfabrication. This process consists of exploiting lithographically defined iron (Fe) catalyst regions, whereon vertically aligned CNT forests are grown in a quartz tube furnace with ethylene gas (C_2H_4 at 750 °C) acting as the carbon feedstock gas (Figure 1a−d). By a similar chemical vapor deposition (CVD) process, performed at an elevated temperature

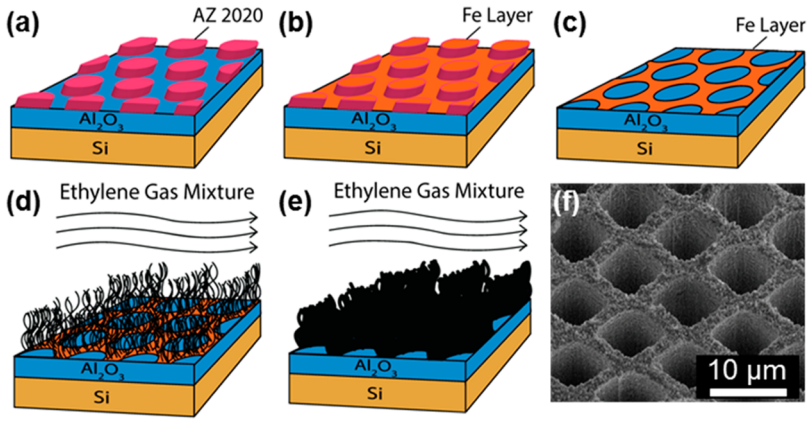

Figure 1. Multistep fabrication process for a CNT-MM. (a) Step 1: photoresist patterned onto Si wafer coated with Al_2O_3. (b) Step 2: thermal evaporation of Fe for CNT growth. (c) Step 3: resultant Fe pattern after solvent lift-off process to obtain hydraulic diameters of 4.025 μm. (d) Step 4: CVD growth of high-aspect ratio CNT-MMs ($\sim$600 μm height) with an ethylene gas mixture as the carbon feedstock gas. (e) Step 5: carbon-infiltration of CNT-MM; (f) SEM image of resultant CNT-MM structure.

(900 °C), these CNT forests can be infiltrated with a mixture of graphitic and amorphous carbon (or qother materials) to coat the outer walls of the CNTs (Figure 1e). In the extreme case, nearly all void space between CNTs can be filled with a desired material, thereby forming solid walls patterned according to the existing CNT layout during growth.[24] The variable porosity of the CNT structures is controlled in part by the exposure time of these structures to the infiltration process. Figure 1f shows a representative *carbon*-infiltrated CNT-MM (CNT is herein taken to mean "carbon-infiltrated CNT") with low-porosity sidewall surfaces. The precise patterning capabilities of photolithography and the macro-scale growth size of CNTs, in conjunction with the added structural versatility afforded by CNT-templated microfabrication, allows for the creation of a variety of high aspect ratio, nanocomposite materials of varying porosity/composition with enhanced structural integrity.[24,41]

The CNT-MMs studied in this work were patterned using a close-packed, diamond-shaped channel mask with a hydraulic diameter of 4.025 μm and minimum wall thickness of $\sim$2.0 μm. Samples grown under the prescribed CNT-templated microfabrication parameters (see Methods) are approximately 600 μm thick with channel aspect ratios of 150:1. Reactive ion etching (RIE) is used to remove the carbon floor layer formed at the base of the CNT-MM against the substrate during the CVD infiltration process. The RIE process also serves to enhance subsequent metallic deposition; therefore, the face opposite the carbon floor layer was also etched.[42,43]

Integration of Electroless Pt Urchin Catalyst. Previous work, including our own, indicates that nanostructured morphologies can be tuned and subsequently exploited to enhance electrocatalytic performance.[42,44,45] Specifically, "needle-like" or "urchin-like" structures display favorable electrocatalytic activity because of their large surface area and desirable geometry (corners, edges, *etc.*).[46] It has been shown that this morphology is likewise desirable for H_2O_2 decomposition,[7] and can be achieved by chemically depositing Pt under conditions of low solution pH ($\lesssim$ 2.5) and high Pt loading concentration ($\gtrsim$ 20% [w/w] Pt−C) resulting in growth of dense Pt nanowires (approximately 10−30 nm in length and 3−4 nm in diameter) on nonporous, singular carbon spheres,[37,39] carbon nanotubes,[35] and cellulose paper[7] as well as three-dimensional graphene.[38]

We follow a similar approach to deposit highly catalytic urchin-like Pt nanoparticles onto the CNT-MMs and even demonstrate the ability to deposit the Pt deep within the CNT microchannels. This electroless deposition is performed on a per-mass basis and involves CNT-MM submersion in a static solution of low pH (<1.5) and high Pt molarity (H_2PtCl_6. $(H_2O)_6$ at $\sim$10 mm) for each deposition (see Methods). Dense coverage of urchin-like Pt nanoparticles is produced as the reduction time of the Pt precursor is increased. This is realized when there is an abundance of H^+ ions in solution (*i.e.*, low pH).[7] Given that no base additives were employed, solution pH was inversely related to Pt molarity. Thus, for a given volume of solution, the desired Pt nanoparticle morphology and density was obtained by increasing the Pt−C loading of the solution (25−30% [w/w] Pt−C) and maintaining a low solution pH (<1.5).

The resultant Pt nanoparticle morphology and density was verified by imaging the Pt-CNT-MMs *via* SEM (Figure 2). This imaging reveals that the entry region sidewalls of a Pt-CNT-MM are uniformly covered with dense urchin-like Pt clusters (Figure 2a), a Pt morphology that resembles those produced in 60% [w/w] Pt−C solution and 2.5 pH loadings by Meng *et al.*[37] Around these entry regions, Pt clusters are observed to protrude from the sidewall into the microchannel by as much as 400 nm. The apparent roughness that these clusters, and their urchin-like structure, add to the microchannels will serve to facilitate additional fuel/catalyst interaction. Inspection of

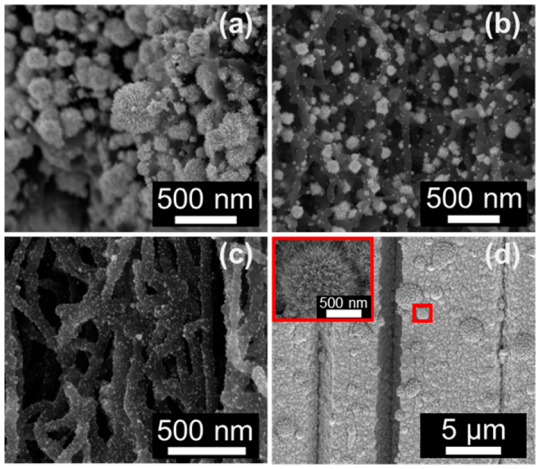

Figure 2. Sample SEM images of fabricated Pt-CNT-MMs. Pt nanoparticle morphology at (a) the microchannel entrance of Pt-CNT-MM, (b) approximately 25 μm into the microchannel, (c) and at the axial center (~280 μm; half the thickness of the CNT-MM sample) of the microchannel. (d) Total coverage along periphery of Pt-CNT-MM with inset showing the urchin-like morphology and arrangement of the deposited Pt.

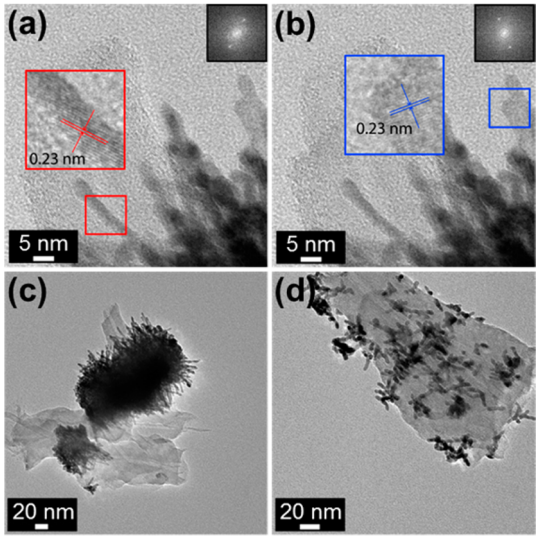

Figure 3. TEM images of Pt-CNT-MM sample. (a) TEM image showing lattice spacing of a synthesized Pt nanowire with Fast Fourier Transform (FFT) inset. (b) Same TEM image showing the lattice spacing of the Pt nanowire on the same cluster but having different crystal plane orientation with FFT inset. (c) Fragment having dense Pt cluster coverage and large growth size, similar to the entrance region of Pt-CNT-MM microchannels. (d) Fragment having less dense urchin-like Pt cluster coverage and smaller growth size, similar to the central interior of Pt-CNT-MM.

Figure 2b,c, taken at successively longer distances (approximately 25 and 280 μm, respectively) into the CNT-MM microchannel, also reveal a uniform spread of Pt catalyst ranging in maximum centripetal protrusion lengths of approximately 120 and 13 nm, respectively. Hence, the size of urchin-like Pt nanowires near the midpoint of each microchannel is considerably smaller than their entry-region counterparts. Nevertheless, evidence of Pt coverage in the axial center of the channel indicates that static Pt deposition is indeed capable of reaching even the most inward portions of the CNT microchannels. Furthermore, SEM imaging of a peripheral region of the Pt-CNT-MMs shows the high affinity of Pt precursor to the O_2 etched CNT-MM structure (Figure 2d). Comparison of the lightly coated inner regions of the Pt-CNT-MM against the densely coated peripheral regions suggest that exposure to the bulk Pt solution enhances Pt coverage, and thus the deposition process is likely diffusion-limited near the axial center of the channel.

TEM Imaging. High-resolution TEM was used to confirm the deposition of Pt nanoparticles onto CNTs, as well as further characterize the dimensions of the Pt nanowires. Characterizing the Pt-CNT-MM by TEM reveals a *d*-spacing between (111) planes of 0.23 nm, confirming that the deposited nanoparticles are Pt (Figure 3a,b).[7,39,47,48] TEM analysis further confirms that the larger Pt urchins have nanowires with lengths of up to 30 nm, which are comparable to lengths reported by Sun *et al.*, and three times longer than those reported by Meng *et al.* on carbon nanotubes and carbon powder, respectively.[35,37] Morphologies of this type, as illustrated in Figure 3c, dominate the *entry regions* of the Pt-CNT-MM microchannels whereas smaller clusters, as illustrated in Figure 3d, fill the central interior. It is also seen that urchin-like Pt nanowires in the *central interior* are half this maximum length, or approximately 15 nm. Pt nanowire diameters measured in both of the aforementioned studies, however, coincide with the 3 nm dimension typically observed here. It is also interesting to note that while average Pt nanowire dimensions (length and diameter) are consistent between clusters at comparable regions along the Pt-CNT-MM channels, the orientation of their (111) planes vary drastically between nanowires, regardless of region and cluster.

Hydrophobicity of Pt-CNT-MMs. Because of their high surface energy and micro/nanoscale surface roughness, CNT structures are natively hydrophobic.[49] Introducing capillary action *via* hydrophilic enhancement of CNTs facilitates intimate contact between fuel (an aqueous reagent) and catalyst, thereby lending to improved fuel decomposition rates. In order to provide hydrophilic enhancement without jeopardizing the structural integrity of the Pt-CNT-MM, we sought a controllable hydrophilic enhancement scheme, suitable to CNT structures.

Studies have shown that the hydrophobic disposition of CNT substrates can be altered by ultraviolet assisted ozone treatment,[50] RIE,[51,52] chemical oxidation and subsequent functionalization,[53] chemical etching,[54,55] and by patterning the CNTs to form macroscale hydrophobic topologies.[49,56] Among these, O_2 RIE was deemed most favorable as it allows for a controllable means of modifying the CNT surfaces to be hydrophilic.[42,52] Accordingly, each CNT-MM was exposed to a brief O_2 etch after growth to improve the penetration

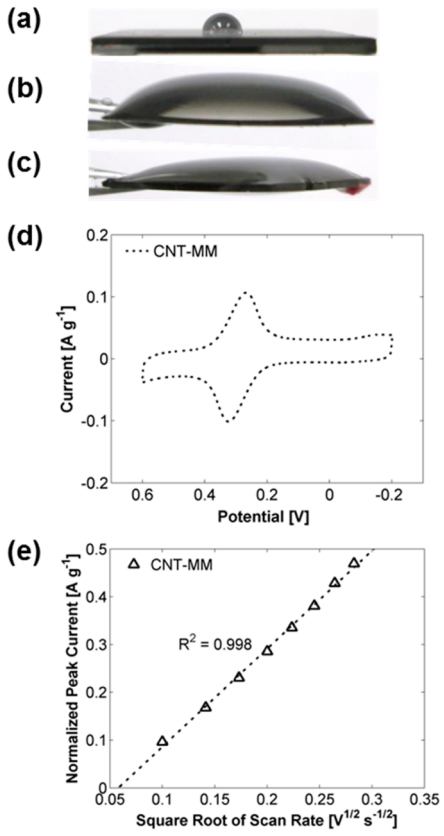

Figure 4. Images of ultrapure water droplet(s) on a CNT-MM at various stages of fabrication; all images taken at same magnification. Water droplet (a) on a CNT-MM before O_2 RIE, showing hydrophobic nature of CNTs; (b) wicking through and dispensing on top of an O_2 RIE etched CNT-MM, showing a hydrophilic nature; and (c) wicking through and dispensing on top of a Pt-CNT-MM, also exhibiting hydrophilic response. (d) CV characterization of CNT-MM sample within ferricyanide mediator solution (4 mm $Fe(CN)_6^{3-}$ and 1 M KNO_3). Representative cyclic voltammogram (current normalized by sample mass) for CNT-MM sample. (e) Plot of the magnitude of the normalized anodic peak current *vs* the square root of the scan rate for a CNT-MM sample, indicating that the transport of ferricyanide to the CNT-MM surface is a diffusion-controlled process.

of aqueous solution into the CNT-MM pores during Pt deposition (see Methods).

A study of the hydrophobic nature of the CNT-MMs was conducted during each stage of the fabrication process. Ultrapure water droplets (10 μL) were dispersed onto separate regions across the surface of a CNT-MM sample before O_2 etching. The water droplets did not appear to wet the CNT-MM channels at any appreciable rate indicating that the surface appeared to be hydrophobic (Figure 4a). This observation was confirmed as the wetting angle of each droplet was measured using a Ramé–Hart precision contact angle goniometer, and was found to have an average value of 110.6 $\pm$ 2.1°. This angle is indicative of a hydrophobic surface,[57] but is lower than the reported water contact angles for CNTs given in related studies.[49,52,53] This discrepancy is likely caused by the smooth graphitic/amorphous carbon coating on the outer walls and caps of the CNTs.

Hydrophobicity tests for post O_2 etched CNT-MM samples revealed hydrophilic behavior as water was observed to spread along the top surface of the membrane and then wick through to the bottom surface of the membrane (Figure 4b); similar hydrophilic behavior was exhibited by the Pt-CNT-MM samples (Figure 4c). If the channel sidewalls were hydrophobic at these stages, aqueous solution would not fill a small channel of this diameter due to the inability to overcome the Laplace pressure. As a result of the spreading and capillary action, no contact angles are reported for either the O_2 etched CNT-MM samples or Pt-CNT-MM samples. These wetting observations support the additional characterization by electrochemical means (which are aqueous-based), as well as subsequent use in propulsion generation where aqueous-based fuel (*i.e.*, H_2O_2) effectively penetrate the pores of the Pt-CNT-MM for catalysis.

Surface Area Analysis. CV was employed to quantify the electroactive surface area for CNT-MMs fabricated under prescribed conditions (see Methods). CV tests were conducted for CNT-MM samples acting as the working electrode, a Ag/AgCl electrode acting as the reference electrode and a coiled Pt wire as the counter electrode. Initial tests were performed using a ferricyanide solution acting as mediator (see Methods).

Electroactive surface areas (EASAs) were calculated using the Randles–Sevcik equation, eq 1, where i_p is the peak redox current (A), n is the number of electrons transferred per redox reaction, A is the EASA (cm^2), D is the mediator diffusion coefficient (6.7×10^{-6} cm^2 s^{-1} for a ferricyanide solution of 4 mm $Fe(CN)_6^{3-}$ and 1 M KNO_3),[58,59] c is the solution concentration (mol cm^{-3}), and v is the potential scan rate (V s^{-1}).[60] CVs were obtained with a potential scan that was cycled between −0.2 and 0.6 V *vs* the Ag/AgCl reference electrode with a scan rate of 10 mV s^{-1} (Figure 4d).

$$i_p = 2.686 \times 10^5 n^{3/2} A c D^{1/2} v^{1/2} \quad (1)$$

To allow for comparison between CNT-MMs of any dimension as well as account for variations in growth across the CNT-MM surface, all CV data was normalized according to sample mass. Hence, EASA calculations were used to determine the electroactive specific surface area (SSA, EASA per unit mass) for each sample. Three CNT-MM test samples were shown to have an average SSA of 293 $\pm$ 28 cm^2 g^{-1}.

Repeating the CV testing for a given CNT-MM sample under varying scan rates revealed a linear relationship between the magnitude of the normalized anodic peak current and the square root of the scan rate for the CNT-MM sample within the ferricyanide mediator solution (Figure 4e). This linear correlation (R^2 values >0.99) suggests that the redox reaction of ferricyanide at the surface is a diffusion-controlled process for CV in a static environment.[61−63] Figure S1

TABLE 1. Comparative BET Surface Area Values

structure	BET surface area ($m^2\ g^{-1}$)	reference
pristine CNTs	131	64
polycarbonate monolith	69	65
CNT-MM	**61**	this work
polyacrylonitrile membrane	39	66
zirconia microtube	23	67

shows comparative plots for CNT-MM and Pt-CNT-MM samples.

A micromeritics ASAP 2010 system was used to further characterize the surface area of the CNT-MM samples. It was found that the CNT-MM samples exhibited a type II nitrogen adsorption isotherm indicative of a macroporous material, with an average calculated BET surface area of 61 $m^2\ g^{-1}$ and a pore volume of 0.118 $cm^3\ g^{-1}$ (Figure S2). Table 1 shows the average calculated BET surface area for CNT-MM samples with comparison to similar structures. Most notably, the BET surface area for the CNT-MMs is approximately half that of pristine CNTs. This is likely attributable to the carbon-infiltration step of the CNT-MM fabrication process, which not only contributes additional mass throughout the structure, but may also cause a reduction in surface area by joining adjacent CNTs. However, the infiltration procedure allows for controllable porosity (mass/surface area) and improved structural integrity.

Hydrogen Peroxide Decomposition. The effectiveness and durability of catalysts for H_2O_2 decomposition is dependent upon multiple factors including material composition, surface area, and reaction temperature. Namely, catalytic performance is defined by its ability to reduce the activation energy required for a given chemical reaction. A variety of catalysts have been developed for lowering the activation energy associated with H_2O_2 decomposition including metal catlaysts[68,69] (*e.g.*, Pt, Pd, Au and Ag) as well as metal oxide catalysts[70−72] (*e.g.*, MnO2, Fe_2O_3, $K_2Cr_2O_7$). Although highly effective at lowering the activation energy of H_2O_2 decomposition, metal oxide catalysts are consumed during H_2O_2 decomposition and therefore would not be able to provide recurring thrust for MUV propulsion. Thus, metal catalysts were chosen for this work. The effectiveness of metal catalysts for H_2O_2 decomposition is proportional to the exposed catalyst surface area. In the case of Pt catalysts, more exposed metal correlates to more free catalytic sites available for Pt-(OH) and Pt-(H) binding—two reactions that are involved in the eight kinetic steps in H_2O_2 decomposition with Pt metal catalysts.[73] Furthermore, the reaction rate for the decomposition of H_2O_2 tends to dramatically increase as the temperature of the exothermic reaction increases. This phenomenon is due to the autodecomposition of H_2O_2 at elevated temperatures and to the fact that oxygen solubility remains low even at higher temperatures.[74] Hence the reaction rates of H_2O_2 decomposition tend to increase due to the conflation of both increased surface area and reaction temperature.

Transport processes may also alter the performance of the Pt-CNT-MM catalysts, including the following: transport of reactants from the main fuel stream to the Pt-CNT-MM surface; transport of reactants within the CNT microchannels to the Pt metal surface; adsorption/desorption of reactants/products at the Pt metal surface; transport of desorbed products from the Pt metal through the CNT microchannels; and transport of desorbed products from within the CNT microchannels to the main stream of fluid.[75] Consequently, the activation energy can change according to the rate of flow introduced into the reaction chamber. Therefore, we report an "effective activation energy" of the Pt-CNT-MM as measured within a convective fuel flow field to mimic, in part, the convective flow field that would be experienced in an actual MUV reaction chamber. Many researchers have not considered the impact of convection on activation energy and often the conditions of fluid stirring are not provided though present during testing. The activation energy provided by others under flowing conditions is equivalent to the effective activation energy defined here, though specific to the conditions of the flow field.

The effective activation energy (E_a) required for H_2O_2 decomposition by the micro/nanostructured Pt-CNT-MMs was empirically determined. H_2O_2 decomposition testing was performed on three replicate Pt-CNT-MM samples (referred to as Samples A, B, and C), each being fabricated as described in the Methods section. Each sample was exposed to 1% [w/w] H_2O_2 solution at three different temperatures (0, 17.5 and 35 °C) in a test flask while the differential pressure (see Methods), resulting from O_2 generation during decomposition of H_2O_2, was monitored eq 2.

$$2H_2O_2 \rightarrow 2H_2O(l) + O_2(g) \qquad (2)$$

The measured differential pressure generated by the reaction products (taken as the average of two or more test runs per sample) was plotted for comparison against two distinct control samples, both tested at 35 °C (Figure 5a). These control samples (referred to as "Samples D and E") were fabricated following the same procedure as for Samples A, B, and C, but received no Pt deposition. As can be seen, Samples A, B, and C generate significantly more pressure than Samples D and E, despite being tested at a lower (less favorable) temperature. Furthermore, negligible pressure rise was observed for the uncoated samples, demonstrating that catalytic performance of Pt-CNT-MMs toward H_2O_2 is strongly dependent on the presence of Pt nanourchins deposited onto the MWCNT microstructure.

Differential pressure data shown in Figure 5a, for Samples A, B, and C, were used in conjunction with the

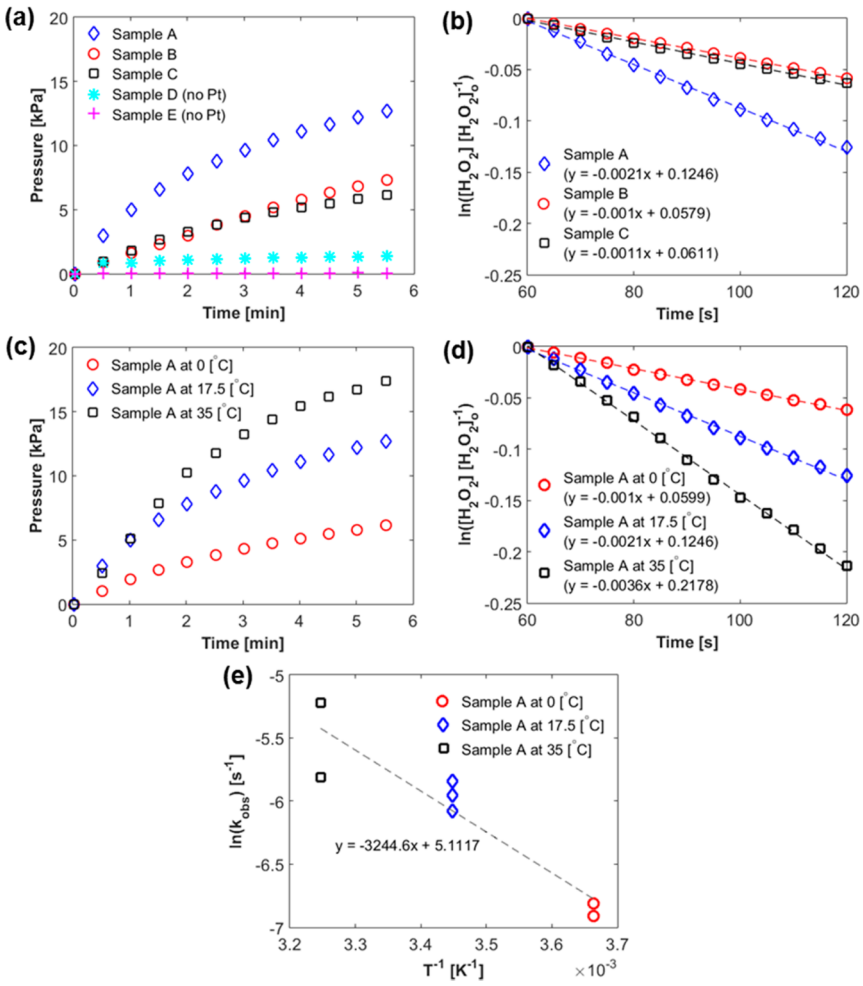

Figure 5. Effective activation energy data for CNT-MM and Pt-CNT-MM samples. (a) Measured differential pressure *vs* time data taken as the average of two or more test runs per sample at 17.5 °C for Pt-CNT-MM Samples A, B, and C, as well as for CNT-MM Samples D and E at 35 °C; data recorded at 1 Hz, sample data shown at 0.033 Hz. (b) Reaction rate plots calculated according to eq 3, using data from (a) and shown at 0.2 Hz. (c) Measured differential pressure *vs* time data taken as the average of two or more tests for Sample A, performed at three temperatures (0, 17.5 and 35 °C); data recorded at 1 Hz, sample data shown at 0.033 Hz. (d) Reaction rate plots calculated according to eq 3, using data from (c) and shown at 0.2 Hz. (e) Plot of the natural log of the Arrhenius Equation for each test run of Sample A with slope used to determine effective activation energy. Dashed lines represent linear curve fits of the data, with equations provided for panels (b), (d) and (e). Goodness of fit values for (b) and (d) are $R^2 > 0.996$ and for (e) is $R^2 = 0.867$.

ideal gas law ($PV = nRT$), to determine the number of moles of O_2 released during the reaction (n), where P is the measured differential pressure (kPa), V is the volume of the flask (125 mL) R is the ideal gas constant (8.314 J mol^{-1} K^{-1}), and T is the bath temperature for the flasks (K). Using this data, in accordance with stoichiometry associated with eq 2, the quantity of H_2O_2 decomposed by the catalyst was determined. The reaction rate constant for the decomposition of H_2O_2 can be determined by the following first-order reaction equation[76]

$$\ln\left(\frac{[H_2O_2]}{[H_2O_2]_0}\right) = -k_{obs}t \qquad (3)$$

where $[H_2O_2]$ is the quantity of hydrogen peroxide remaining in solution at time t, $[H_2O_2]_0$ is the initial quantity of H_2O_2 in solution, and k_{obs} is the reaction rate constant (s^{-1}) over time. Figure 5b illustrates the ratio of the remaining fuel to the initial quantity of fuel (10 mL of 1% [w/w] H_2O_2 solution), used to determine the reaction rate constant for the data in Figure 5a according to eq 3. To avoid inclusion of initial noise in the pressure data, measurements taken between 60 and 120 s were used for all calculations of k_{obs}. Additional testing of Sample A under three different temperatures (0 °C, 17.5 °C and 35 °C) illustrated higher observed decomposition rates with increasing temperature (Figure 5c,d).

The natural log of the Arrhenius equation, eq 4, with the calculated observed reaction rate constants are used to calculate the effective activation energy.

$$\ln(k_{obs}) = -\frac{E_a}{R}\frac{1}{T} + \ln(A) \qquad (4)$$

Here, E_a is the effective activation energy of the catalyst (J mol^{-1}), and A is the pre-exponential factor

TABLE 2. Average H_2O_2 Decomposition Kinetics for the Pt-CNT-MMs[a]

temperature (°C)	k_{obs} ($s^{-1} \times 10^{-3}$)	E_a (kJ mol^{-1})	A (s^{-1})	ΔS (J mol^{-1} K^{-1})
0	1.0 ± 0.1	26.96 (33.70 < E_a < 20.12)	165.84	42.47 (±34.36)
17.5	2.1 ± 0.3			
35	3.6 ± 1.7			

[a] Range of possible values and one standard deviation shown in parentheses for E_a and ΔS, respectively.

(s^{-1}). By plotting the natural log of the observed reaction rate constant for each test run as a function of inverse temperature for Sample A, the effective activation energy (26.96 kJ mol^{-1}) was acquired from the slope of the linear fit of the data (Figure 5e). Error associated with the effective activation energy value is bounded by the upper and lower limits of 33.70 and 20.12 kJ mol^{-1}, respectively, calculated using slopes of the extreme cases presented in Figure 5e.

Table 2 provides an overview of the calculated decomposition kinetics for a Pt-CNT-MM (Sample A), including the entropy of activation, ΔS (J mol^{-1} K^{-1}; where $\Delta S = R \cdot \ln(A)$). This reported effective activation energy of 26.96 kJ mol^{-1} seems to improve upon similar nanostructured surfaces such as those comprised of graphene (28.8 kJ mol^{-1})[77] and Pt/palladium nanoparticles on Nafion (34.0−36.3 kJ mol^{-1}).[74] Furthermore, the effective activation energy is lower than our previous Pt-paper catalyst (29.5 kJ mol^{-1})[7] where similar Pt nanourchins were deposited on cellulose sheets—such improvement is most likely due to the higher surface area achieved by the three-dimensional architecture created by the CNT microchannels of the CNT-MM as opposed to the planar structure of the cellulose sheets.

MUV Platform and Propulsion Testing. An MUV test submersible was created in order to test the capability of the developed Pt-CNT-MMs to produce thrust *via* H_2O_2 decomposition. The developed MUV test submersible, fabricated *via* a 3D printer (see Methods), is capable of housing eight inline Pt-CNT-MM samples (each with a square planar surface area of 2.867 cm^2; Figure 6a). Measurement of the propulsive thrust generated by the decomposition of H_2O_2 by Pt-CNT-MMs housed within the test submersible was performed by attaching a strain gauge to the mounting rod holding the test submersible. Syringe-fed tubing was secured to the inlet port of the test submersible for the supply of H_2O_2 fuel, and the assembly was then lowered into a water tank for testing (Figure 6b).

Heterogeneous catalytic reactions are heavily dependent on the mass transfer of reactant (fuel) to the catalytic surface.[78] Thrust generated *via* decomposition of H_2O_2 fuel is therefore dependent on the introduction rate of the fuel to the Pt-CNT-MM surface.

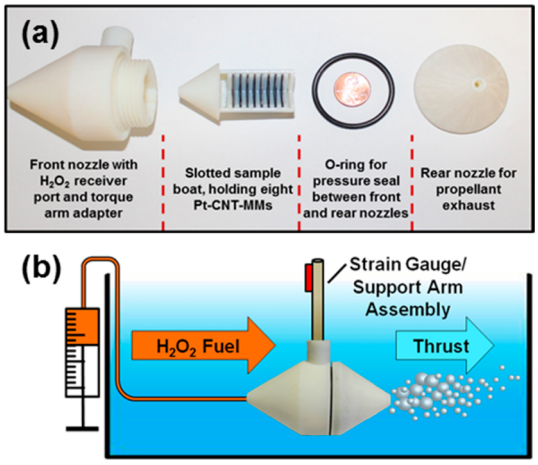

Figure 6. Test submersible assembly and water tank setup for monitoring thrust capability. (a) Optical image displaying disassembled test submersible parts with corresponding descriptions and (b) schematic illustrating assembled test submersible and water tank setup.

This introduction rate can be modified in three ways: by changing the fuel concentration, changing the fuel flow rate, and/or by changing the available catalytic surface area. Accordingly, propulsion testing was performed using three different H_2O_2 concentrations (20, 35, and 50% [w/w]), each at a given average flow rate (10 mL s^{-1}) for one, two, four, six, and eight Pt-CNT-MMs. Also, a manually driven (high burst) flow rate using 50% [w/w] H_2O_2 was conducted for one, four, and eight Pt-CNT-MMs (see Supporting Video S1). As a control, water was injected into the submersible reaction chamber, holding eight Pt-CNT-MMs, at the highest flow rate tested (manually driven burst) (see Supporting Video S2). With no appreciable thrust observed for this water control run, all measured thrust was attributed to the decomposition of H_2O_2. Reported thrust values for each combination of test conditions were taken from the average of two or more tests.

Measured thrust under the 10 mL s^{-1} flow conditions is shown in Figure 7a. Comparison of the corresponding 20 and 50% [w/w] H_2O_2 cases demonstrates that an increase in fuel concentration lends to greater generated thrust. Initially, it is also observed that with an increased quantity of Pt-CNT-MMs (increased catalytic surface area), there is a notable increase in measured thrust. For the 20 and 35% [w/w] H_2O_2 test runs, no appreciable thrust is observed by having greater than six Pt-CNT-MMs. This may be due to the H_2O_2 fuel approaching total decomposition within the reaction chamber of the test submersible for these conditions.

Thrust produced at a fixed fuel concentration (50% [w/w] H_2O_2) for varying flow rates is presented in Figure 7b. It is shown that both the 10 mL s^{-1} and manually driven flow rates exhibit monotonically increasing thrust per additional Pt-CNT-MM, suggesting incomplete fuel decomposition. It is anticipated that higher thrusts would be attained by the addition of

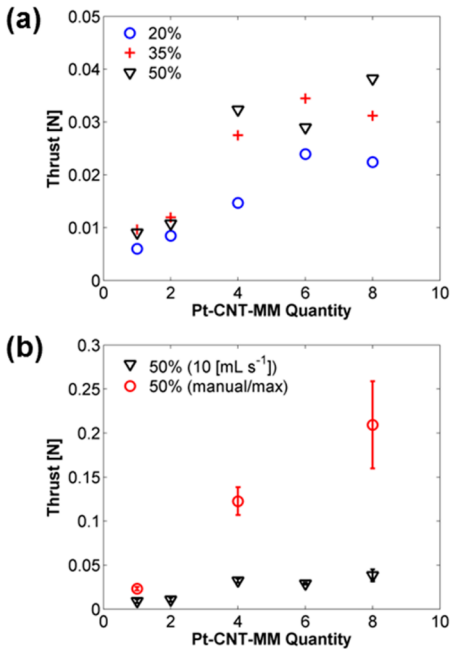

Figure 7. Thrust measurement plots for H_2O_2 decomposition-driven propulsion. (a) Varying H_2O_2 concentration (20, 35, and 50% [w/w] H_2O_2) per fixed flow rate (10 mL s^{-1}); 20 and 35% [w/w] H_2O_2 fuel approaching total decomposition with addition of Pt-CNT-MM samples. (b) Fixed H_2O_2 fuel concentration (50% [w/w] H_2O_2) per varied flow rates (10 mL s^{-1} and manually driven high burst flow); illustrates thrust generation dependence on H_2O_2 fuel flow rate.

more inline Pt-CNT-MM samples until total fuel decomposition occurs. Ultimately, for the manually driven flow rate, a maximum thrust of 209 ± 49 mN was achieved using eight Pt-CNT-MMs. It is also observed that, for the same number of Pt-CNT-MM samples and H_2O_2 fuel concentration, the manually driven flow rate produces significantly greater thrust than that for 10 mL s^{-1}, suggesting a flow rate dependent thrust.

In summary, it has been shown that an increase in H_2O_2 fuel concentration, catalytic surface area, and flow rate all contribute to additional thrust, demonstrating that thrust generated by catalysis is dependent on the introduction rate of H_2O_2 fuel to the Pt-CNT-MM structure. Further, it has been demonstrated that the fuel can approach complete decomposition for a given fuel concentration and flow rate by addition of Pt-CNT-MMs.

CONCLUSION

CNT-templated microfabrication techniques can be used to fabricate carbon-infiltrated multiwalled CNT scaffolds composed of highly ordered and aligned microchannels with desired geometry. Furthermore, urchin-like Pt nanoparticles can then be deposited onto, and throughout, the entirety of the CNT-MMs to provide a high aspect ratio catalytic microstructure for the enhanced propulsion of MUVs. While many publications report Pt nanoparticle deposition onto carbon structures, this work is the first to demonstrate Pt nanoparticle deposition onto carbon-infiltrated MWCNTs. Additionally, this work reports the successful union between CNT-templated microfabrication and chemical deposition of nanoparticles. Such an electroless deposition technique is capable of depositing nanoparticles ~200 μm deep within the pores of the CNT microchannels.

Post O_2 etched CNT-MM and Pt-CNT-MM samples demonstrate excellent hydrophilic behavior, which is well-suited for aqueous-based characterization and propulsion methods and is a significant shift from the hydrophobic nature of nonetched CNT-MMs. CNT-MM samples achieved an average electroactive surface area of 293 ± 28 cm^2 g^{-1} within a ferricyanide based CV solution. Additionally, effective activation energy testing of Pt-CNT-MM samples revealed a favorable performance of 26.96 kJ mol^{-1}.

The efficacy of Pt-CNT-MMs, functionalized in 25−30% [w/w] Pt−C solution, for the propulsion of MUVs was demonstrated with eight inline Pt-CNT-MMs, exposed to manually driven high burst flows of 50% [w/w] H_2O_2, producing a maximum average thrust of 209 ± 49 mN. This propulsive bursting thrust falls within the milli-newton thrust typically required for MUV propulsion,[7,40] and is shown to be at least 6.5 times greater than that produced by several biomimetic propulsion designs.[79−82] The proposed approach minimizes component exposure to the environment and is comprised of a simple, static architecture relative to other micropropulsion systems. Furthermore, it was shown that additional thrust is attainable by enhancing the introductory rate of the H_2O_2 fuel to the Pt-CNT-MMs, which would effectively increase the locomotive capability of this propulsion system.

Future work will be devoted to optimizing Pt deposition as well as performing depositions in a through-flow environment. Pt-CNT-MM performance will be enhanced by studying the effects of microchannel geometry, porosity and dimensions. Further work will be devoted to quantifying the decomposition rate enhancement by application of these Pt-CNT-MMs in a through-flow environment. It can be expected that such a setup would increase the generated thrust per Pt-CNT-MM and induce earlier total fuel decomposition for a given number of Pt-CNT-MMs at a prescribed flow rate.

METHODS

CNT-MM Fabrication. A 4″ silicon wafer was coated with a thin aluminum oxide film (Al_2O_3, > 30 nm) using e-beam evaporation primarily to act as a barrier to subsequent reactions between the iron layer and the underlying silicon substrate.[24] AZ nLOF2020 photoresist was spun on at 2750 rpm for 60 s and soft baked at 110 °C for 60 s. CNT-MM pore geometry and

dimensions (diamond shape with nominal diagonal dimensions of 4.5 × 9.0 μm) were defined on the wafer by photolithography, and hard baked at 110 °C for 60 s. The photoresist was developed in a lightly agitated, AZ300MIF solution. A thin iron film (Fe, ~7 nm) was thermally evaporated onto the wafer surface as a catalyst for CNT growth. The wafer was sonicated in solvent for >10 min, rinsed with isopropyl alcohol (IPA), and dried with compressed air to remove the entire photoresist layer and portions of the Fe layer in a lift-off process. To protect the wafer during sample dicing, a thin photoresist layer (AZ 3330) was spun on the wafer and soft baked. Typically, samples were diced into 16.93 × 16.93 mm squares using a Disco DAD-320 dicing saw. Variations in test data given by samples diced to smaller dimensions were accounted for by normalizing all results on a per-mass basis. Preparatory to CNT growth, diced samples with patterned Fe were solvent cleaned to remove the protective photoresist layer.

CNT-MM Growth, Release, and Cleaning. After a quality inspection check with an optical microscope, diced samples were placed on a quartz boat in a Lindberg/Blue M Tube Furnace for CNT growth. CNTs were grown for 26 min in flowing hydrogen (H_2, ~216 sccm) and ethylene (C_2H_4, ~280 sccm) at 750 °C. This resulted in a CNT-MM height of approximately 600 μm. CNT-MMs were then coated with carbon in a subsequent infiltration step at 900 °C for 20 min with similar gases and flow rates as those used during CNT growth (H_2 at ~200 sccm and C_2H_4 at ~280 sccm). This resulted in carbon-infiltrated CNTs with diameters of approximately 290 nm. During carbon infiltration, the CNT-MM structure self-released from the wafer substrate. CNT-MMs were exposed to a brief 7 min O_2 plasma etching at 300 W using an Anelva Reactive Ion Etcher (RIE), DEM-451 to remove the carbon floor (additional carbon blocking the base of the CNT-MM channels) and enhance hydrophilicity to improve subsequent deposition of Pt catalyst (5 min for removal of the carbon floor layer; 2 min for opposite face).

Urchin-like Pt Nanoparticle Deposition. Deposition of Pt onto the CNT-MM was performed on a per-mass basis to maintain a 25−30% [w/w] Pt−C solution loading. For a CNT-MM with a mass of 0.1071 g, 122.8 mg chloroplatinic acid hexahydrate was weighed out (37.5% Pt, Sigma-Aldrich 206083) and mixed with 2.0 mL formic acid (88% HCOOH, Macron 2592−05) and 18.0 mL ultrapure H_2O. These chemicals were added to a 50 mL glass beaker (VWR, 89000−198) whereupon their pH level was measured. The pH for this deposition was 1.16, enabling urchin-like nanoparticle growth. Using a slotted Teflon ring for a sample stand, the CNT-MM was positioned vertically in the plating solution. Keeping the sample oriented in this manner ensured that the Pt nanoparticles would nucleate and grow on the carbon substrate rather than precipitating out of solution and simply collecting on the sample face. Because the mass of the CNT-MM was 0.1071 g, the solution molarity (11.80 mm) corresponded to a 30.07% [w/w] Pt−C loading. The beaker was then covered by Parafilm and left until the deposition process was completed, indicated by solution color change from amber to clear. Upon removal from the beaker, and prior to subsequent testing, the sample was submerged in deionized water for at least 5 min and then placed in an Ultra-Clean 100 (3497M-3) dehydration bake oven for a minimum of 8 min.

Electrode Attachment for Cyclic Voltammetry Testing. Duralco 120 silver epoxy was used to attach Nichrome wire to each sample used for CV testing. After the silver epoxy had cured (approximately 24 [hrs]), a chemically inert lacquer coating was applied to the silver joint. CV tests were conducted using a CHI 630E Potentiostat/Galvanostat. A three-electrode cell was setup with the CNT-MM samples acting as the working electrode, a Ag/AgCl electrode acting as the reference electrode and a coiled Pt wire as the counter electrode. Initial tests were performed using a ferricyanide solution acting as mediator. Three cycles were run per sample test through a potential range of −0.2−0.6 V at a scan rate of 10 mV s^{-1}. The peak redox current for each sample was taken as the average of both anodic/cathodic peak currents of the latter two CV cycles. All runs were performed at room temperature.

Nitrogen Gas Adsorption Testing. Nitrogen adsorption analysis was performed on a Micromeritics ASAP 2010 system at 77 K (Micromeritics Instrument Corporation, Norcross, GA). Samples were degassed at 100 °C prior to analysis. Surface area was calculated by the Brunauer−Emmett−Telller (BET) method, pore size was measured by the Barrett−Joyner−Halenda (BJH) method using the adsorption branch of the isotherm, and total pore volume was determined by the single point method at relative pressure (P/P_0) 0.97.

Hydrogen Peroxide Decomposition. Effective activation energy tests, by H_2O_2 decomposition, was conducted using three Pt-CNT-MM samples fabricated following the procedure described previously. Each sample was tested two or more times, after which the pressure data was averaged per sample. The test apparatus consisted of two, 125 mL, round-bottom flasks. One flask was used for the Pt-CNT-MM test environment and the other as a reference environment (Figure 8). Magnetic stir bars were placed inside each flask and rotated at 250 rpm to increase the amount of H_2O_2 contacting the catalytic Pt-CNT-MM samples and mimic, in part, the convective flow environment experienced through injection of H_2O_2 fuel into a MUV. To ensure the flasks were airtight, rubber septums with a rim seal were positioned on each flask. The flasks were placed inside ice or water baths on top of a hot plate stirrer to maintain isothermal conditions during each of the two or more runs per sample (0, 17.5 and 35 °C). To ensure that no steam was produced during testing, such that all generated pressure was due to the release of O_2, a low concentration H_2O_2 solution (1% [w/w] H_2O_2, diluted from 30% [w/w] H_2O_2; Fisher Scientific BP2633−500) was used for all tests. The H_2O_2 solution stock was placed within a 50 mL container and immersed in the respective ice/water baths in order to achieve thermal equilibrium prior to testing. After achieving thermal equilibration, each flask was vented by temporary insertion of an unattached needle and allowed to equilibrate with atmospheric pressure. The amount of O_2 generated during each test was measured as a pressure differential between the testing and reference environments. To measure the pressure differential, an Extech HD750 Differential Pressure Manometer (measuring up to ±5 psi/34.5 kPa) was connected to each flask *via* two high strength silicone tubes

Figure 8. Experimental apparatus used to monitor the increase in pressure due to O_2 generation during H_2O_2 decomposition. Water maintained at a constant temperature holds test and control flasks on a hot plate while a differential pressure monitor measures transient pressure data.

(diameter 0.375 in./9.525 mm). The tubing was connected to the manometer and syringe needles using barbed fittings. The two syringe needles connected to the pressure manometer were inserted into the test and control flasks, respectively, by piercing through the diaphragm of each septa. The differential pressure between the test and control flasks was zeroed before recording data and then measured as a function of time with a laptop computer *via* a USB connection. Finally, 10 mL of the H_2O_2 solution was simultaneously injected into each flask while the magnetic stir bars stirred the solution at 200 rpm. Resultant differential pressure *vs* time data was then used to determine catalyst performance and effective activation energy with the Arrhenius Equation.

MUV Fabrication and Testing. The MUV test submersible was designed with computer aided design software (SolidWorks) and printed with an Objet500 Connex 3D printer with a PMMA like resin. The test submersible was then fitted to a 30.5 in. (0.77 m) rigid arm through screw thread fastening and submerged into a water tank (350 gal). The opposite end of the arm was secured to a torque transducer (Interface model 5350—50:50 oz-in sensor) mounted above the water tank. The transducer reported torque measurements with 0.001 N-m precision along the parallel axis of the test submersible *via* a CPU connection. Force (thrust) measurements were calculated *via* software on the CPU. H_2O_2 was pumped into the reaction chamber *via* a 50 mL syringe connected to the test submersible's reaction chamber *via* high strength silicone tube (dia.: 0.375 in./9.525 mm) that fits over a plastic barbed fitting.

Conflict of Interest: The authors declare no competing financial interest.

Acknowledgment. The authors gratefully acknowledge additional assistance from T. Smith, R. Watt, M. Standing, and J. Farrer for equipment access and training. The authors would like to also recognize funding support from ONR, NRL, and DTRA as well as from the Departments of Mechanical Engineering at Brigham Young University and Iowa State University and the College of Engineering at Iowa State University.

Supporting Information Available: Additional CV test data, N_2 adsorption isotherms, and supporting videos. The Supporting Information is available free of charge on the ACS Publications website at DOI: 10.1021/acsnano.5b02124.

REFERENCES AND NOTES

1. Chen, E.; Sheng-wei, H.; Wei-Han, W.; Jen-Hwa, G. In *Side Scan Sonar Grid Map for Unmanned Underwater Vehicle Navigation*; Institute of Electrical and Electronics Engineers, OCEANS: Waikoloa, 2011.
2. Mohseni, K. Pulsatile Vortex Generators for Low-Speed Maneuvering of Small Underwater Vehicles. *Ocean Eng.* **2006**, *33*, 2209–2223.
3. Kodati, P. *Biomimetic Micro Underwater Vehicle with Ostraciiform Locomotion: System Design, Analysis and Experiments*; ProQuest: Ann Arbor, 2006; pp 1—2.
4. Crimmins, D. M.; Patty, C. T.; Beliard, M. A.; Baker, J.; Jalbert, J. C.; Komerska, R. J.; Chappell, S. G.; Blidberg, D. R. In *Long-Endurance Test Results of the Solar-Powered AUV System*; Institute of Electrical and Electronics Engineers, OCEAN: Boston, 2006.
5. Hobson, B. W.; Bellingham, J. G.; Kieft, B.; McEwen, R.; Godin, M.; Yanwu, Z. In *Tethys-Class Long Range AUVs—Extending the Endurance of Propeller-Driven Cruising AUVs from Days to Weeks*, Autonomous Underwater Vehicles (AUV); The Insitute of Electrical and Electronics Engineers Oceanic Engineering Society: Southampton, 2012.
6. Hyakudome, T.; Tsukioka, S.; Yoshida, H.; Sawa, T.; Ishibashi, S.; Ishikawa, A.; Ishiwata, J.; Watanabe, K.; Nakamura, M.; Aoki, T. In *Autonomous Underwater Vehicle for Surveying Deep Ocean*, Institute of Electrical and Electronics Engineers International Conference; Institute of Electrical and Electronics Engineers: Gippsland, 2009.
7. Claussen, J. C.; Daniele, M. A.; Geder, J.; Pruessner, M.; Makinen, A. J.; Melde, B. J.; Twigg, M.; Verbarg, J. M.; Medintz, I. L. Platinum-Paper Micromotors: An Urchin-Like Nanohybrid Catalyst for Green Monopropellant Bubble-Thrusters. *ACS Appl. Mater. Interfaces* **2014**, *6*, 17837–17847.
8. Rusek, J. J. In *Hydrogen Peroxide for Propulsion and Power Applications: A Swift Perspective*, 2nd International Conference on Green Propellants for Space Propulsion; European Space Agency: Sardinia, 2004.
9. Kim, J.; Nam, D.-G.; Oh, W. Electrochemical Oxidations of Alcohols on Platinum/Carbon Nanotube Composites. *Trans. Electr. Electron. Mater.* **2013**, *14*, 125–129.
10. Watt, G. D. Kinetic Evaluation of the Viologen-Catalyzed Carbohydrate Oxidation Reaction for Fuel Cell Application. *Renewable Energy* **2014**, *63*, 370–375.
11. Wernimont, E. J. In *Monopropellant Hydrogen Peroxide Rocket Systems: Optimum for Small Scale*, 42nd AIAA/ASME/SAE/ASEE Joint Propulsion Conference & Exhibit; AIAA: Sacramento, 2006.
12. Ke, H.; Ye, S.; Carroll, R. L.; Showalter, K. Motion Analysis of Self-Propelled Pt—Silica Particles in Hydrogen Peroxide Solutions. *J. Phys. Chem. A* **2010**, *114*, 5462–5467.
13. Gibbs, J. G.; Zhao, Y. P. Autonomously Motile Catalytic Nanomotors by Bubble Propulsion. *Appl. Phys. Lett.* **2009**, *94*, 163104–163106.
14. Baraban, L.; Makarov, D.; Streubel, R.; Mönch, I.; Grimm, D.; Sanchez, S.; Schmidt, O. G. Catalytic Janus Motors on Microfluidic Chip: Deterministic Motion for Targeted Cargo Delivery. *ACS Nano* **2012**, *6*, 3383–3389.
15. Campuzano, S.; Orozco, J.; Kagan, D.; Guix, M.; Gao, W.; Sattayasamitsathit, S.; Claussen, J. C.; Merkoçi, A.; Wang, J. Bacterial Isolation by Lectin-Modified Microengines. *Nano Lett.* **2011**, *12*, 396–401.
16. Manesh, K. M.; Cardona, M.; Yuan, R.; Clark, M.; Kagan, D.; Balasubramanian, S.; Wang, J. Template-Assisted Fabrication of Salt-Independent Catalytic Tubular Microengines. *ACS Nano* **2010**, *4*, 1799–1804.
17. Mirkovic, T.; Zacharia, N. S.; Scholes, G. D.; Ozin, G. A. Fuel for Thought: Chemically Powered Nanomotors Out-Swim Nature's Flagellated Bacteria. *ACS Nano* **2010**, *4*, 1782–1789.
18. Gao, W.; Sattayasamitsathit, S.; Orozco, J.; Wang, J. Highly Efficient Catalytic Microengines: Template Electrosynthesis of Polyaniline/Platinum Microtubes. *J. Am. Chem. Soc.* **2011**, *133*, 11862–11864.
19. Laocharoensuk, R.; Burdick, J.; Wang, J. Carbon-Nanotube-Induced Acceleration of Catalytic Nanomotors. *ACS Nano* **2008**, *2*, 1069–1075.
20. Soler, L.; Magdanz, V.; Fomin, V. M.; Sanchez, S.; Schmidt, O. G. Self-Propelled Micromotors for Cleaning Polluted Water. *ACS Nano* **2013**, *7*, 9611–9620.
21. Wang, Y.; Hernandez, R. M.; Bartlett, D. J.; Bingham, J. M.; Kline, T. R.; Sen, A.; Mallouk, T. E. Bipolar Electrochemical Mechanism for the Propulsion of Catalytic Nanomotors in Hydrogen Peroxide Solutions. *Langmuir* **2006**, *22*, 10451–10456.
22. Mei, Y.; Huang, G.; Solovev, A. A.; Ureña, E. B.; Mönch, I.; Ding, F.; Reindl, T.; Fu, R. K. Y.; Chu, P. K.; Schmidt, O. G. Versatile Approach for Integrative and Functionalized Tubes by Strain Engineering of Nanomembranes on Polymers. *Adv. Mater.* **2008**, *20*, 4085–4090.
23. Solovev, A. A.; Mei, Y.; Bermúdez Ureña, E.; Huang, G.; Schmidt, O. G. Catalytic Microtubular Jet Engines Self-Propelled by Accumulated Gas Bubbles. *Small* **2009**, *5*, 1688–1692.
24. Hutchison, D. N.; Morrill, N. B.; Aten, Q.; Turner, B. W.; Jensen, B. D.; Howell, L. L.; Vanfleet, R. R.; Davis, R. C. Carbon Nanotubes as a Framework for High-Aspect-Ratio MEMS Fabrication. *J. Microelectromech. Syst.* **2010**, *19*, 75–82.
25. Song, J.; Jensen, D. S.; Hutchison, D. N.; Turner, B.; Wood, T.; Dadson, A.; Vail, M. A.; Linford, M. R.; Vanfleet, R. R.; Davis, R. C. Carbon-Nanotube-Templated Microfabrication of Porous Silicon-Carbon Materials with Application to Chemical Separations. *Adv. Funct. Mater.* **2011**, *21*, 1132–1139.
26. Cho, Y.-R.; Lee, J. H.; Song, Y.-H.; Kang, S.-Y.; Hwang, C.-S.; Jung, M.-Y.; Kim, D.-H.; Lee, S.-K.; Uhm, H.-S.; Cho, K. I.

Photolithography-Based Carbon Nanotubes Patterning for Field Emission Displays. *Mater. Sci. Eng., B* **2001**, *79*, 128–132.
27. Zhang, L.; Shi, T.; Xi, S.; Liu, D.; Tang, Z.; Li, X.; Lai, W. Carbon Nanotube Integrated 3-Dimensional Carbon Microelectrode Array by Modified SU-8 Photoresist Photolithography and Pyrolysis. *Thin Solid Films* **2011**, *520*, 1041–1047.
28. Tasaltin, C.; Basarir, F. Preparation of Flexible VOC Sensor Based on Carbon Nanotubes and Gold Nanoparticles. *Sens. Actuators, B* **2014**, *194*, 173–179.
29. Maruyama, S.; Xiang, R. Chemical Vapor Deposition Growth, Optical, and Thermal Characterization of Vertically Aligned Single-Walled Carbon Nanotubes. *J. Heat Transfer* **2012**, *134*, 1–6.
30. Claussen, J. C.; Franklin, A. D.; Haque, A. U.; Marshall Porterfield, D.; Fisher, T. S. Electrochemical Biosensor of Nanocube-Augmented Carbon Nanotube Networks. *ACS Nano* **2009**, *3*, 37–44.
31. Amama, P. B.; Ogebule, O.; Maschmann, M. R.; Sands, T. D.; Fisher, T. S. Dendrimer-Assisted Low-Temperature Growth of Carbon Nanotubes by Plasma-Enhanced Chemical Vapor Deposition. *Chem. Commun.* **2006**, 2899–2901.
32. Choi, Y. C.; Shin, Y. M.; Lee, Y. H.; Lee, B. S.; Park, G.-S.; Choi, W. B.; Lee, N. S.; Jong-Min, K. Controlling the Diameter, Growth Rate, and Density of Vertically Aligned Carbon Nanotubes Synthesized by Microwave Plasma-Enhanced Chemical Vapor Deposition. *Appl. Phys. Lett.* **2000**, *76*, 2367–2369.
33. Peng, Y.; Hu, Y.; Wang, H. Patterned Deposition of Multi-Walled Carbon Nanotubes on Self-Assembled Monolayers. *Chin. Sci. Bull.* **2006**, *51*, 147–150.
34. Lalwani, G.; Kwaczala, A. T.; Kanakia, S.; Patel, S. C.; Judex, S.; Sitharaman, B. Fabrication and Characterization of Three-Dimensional Macroscopic All-Carbon Scaffolds. *Carbon* **2013**, *53*, 90–100.
35. Sun, S.; Yang, D.; Zhang, G.; Sacher, E.; Dodelet, J.-P. Synthesis and Characterization of Platinum Nanowire–Carbon Nanotube Heterostructures. *Chem. Mater.* **2007**, *19*, 6376–6378.
36. Sun, S.; Zhang, G.; Geng, D.; Chen, Y.; Banis, M. N.; Li, R.; Cai, M.; Sun, X. Direct Growth of Single-Crystal Pt Nanowires on Sn@CNT Nanocable: 3D Electrodes for Highly Active Electrocatalysts. *Chem.—Eur. J.* **2010**, *16*, 829–835.
37. Meng, H.; Xie, F.; Chen, J.; Sun, S.; Shen, P. K. Morphology Controllable Growth of Pt Nanoparticles/Nanowires on Carbon Powders and its Application as Novel Electro-Catalyst for Methanol Oxidation. *Nanoscale* **2011**, *3*, 5041–5048.
38. Sattayasamitsathit, S.; Gu, Y.; Kaufmann, K.; Jia, W.; Xiao, X.; Rodriguez, M.; Minteer, S.; Cha, J.; Burckel, D. B.; Wang, C.; Polsky, R.; Wang, J. Highly Ordered Multilayered 3D Graphene Decorated with Metal Nanoparticles. *J. Mater. Chem. A* **2013**, *1*, 1639–1645.
39. Sun, S.; Jaouen, F.; Dodelet, J.-P. Controlled Growth of Pt Nanowires on Carbon Nanospheres and Their Enhanced Performance as Electrocatalysts in PEM Fuel Cells. *Adv. Mater.* **2008**, *20*, 3900–3904.
40. Watson, S. A.; Green, P. N. In *Propulsion Systems for Micro-Autonomous Underwater Vehicles (μAUVs)*, Robotics Automation and Mechatronics (RAM), 2010 Institute of Electrical and Electronics Engineers Conference, Singapore, **2010**.
41. Hanna, B. H.; Fazio, W. C.; J.D, T.; Lund, J. M.; Wood, T. S.; Davis, R. C.; Vanfleet, R. R.; Jensen, B. D. Mechanical Property Measurement of Carbon Infiltrated Carbon Nanotube Structures for Compliant Micromechanisms. *J. Microelectromech. Syst.* **2014**, *23*, 1330–1339.
42. Claussen, J. C.; Kumar, A.; Jaroch, D. B.; Khawaja, M. H.; Hibbard, A. B.; Porterfield, D. M.; Fisher, T. S. Nanostructuring Platinum Nanoparticles on Multilayered Graphene Petal Nanosheets for Electrochemical Biosensing. *Adv. Funct. Mater.* **2012**, *22*, 3399–3405.
43. Wang, S. C.; Chang, K. S.; Yuan, C. J. Enhancement of Electrochemical Properties of Screen-Printed Carbon Electrodes by Oxygen Plasma Treatment. *Electrochim. Acta* **2009**, *54*, 4937–4943.
44. Soleymani, L.; Fang, Z.; Sargent, E. H.; Kelley, S. O. Programming the Detection Limits of Biosensors through Controlled Nanostructuring. *Nat. Nanotechnol.* **2009**, *4*, 844–848.
45. Soleymani, L.; Fang, Z.; Sun, X.; Yang, H.; Taft, B. J.; Sargent, E. H.; Kelley, S. O. Nanostructuring of Patterned Microelectrodes To Enhance the Sensitivity of Electrochemical Nucleic Acids Detection. *Angew. Chem., Int. Ed.* **2009**, *48*, 8457–8460.
46. Yao, Z.; Zhu, M.; Jiang, F.; Du, Y.; Wang, C.; Yang, P. Highly Efficient Electrocatalytic Performance Based on Pt Nanoflowers Modified Reduced Graphene Oxide/Carbon Cloth Electrode. *J. Mater. Chem.* **2012**, *22*, 13707–13713.
47. Tsen, S. C. Y.; Crozier, P. A.; Liu, J. Lattice Measurement and Alloy Compositions in Metal and Bimetallic Nanoparticles. *Ultramicroscopy* **2003**, *98*, 63–72.
48. Kwak, D.-H.; Lee, Y.-W.; Lee, K.-H.; Park, A.-R.; Moon, J.-S.; Park, K.-W. One-Step Synthesis of Hexapod Pt Nanoparticles Deposited on Carbon Black for Improved Methanol Electrooxidation. *Int. J. Electrochem. Sci.* **2013**, *8*, 5102–5107.
49. Lu, S. H.; Ni Tun, M. H.; Mei, Z. J.; Chia, G. H.; Lim, X.; Sow, C.-H. Improved Hydrophobicity of Carbon Nanotube Arrays with Micropatterning. *Langmuir* **2009**, *25*, 12806–12811.
50. Wang, H. Z.; Huang, Z. P.; Cai, Q. J.; Kulkarni, K.; Chen, C. L.; Carnahan, D.; Ren, Z. F. Reversible Transformation of Hydrophobicity and Hydrophilicity of Aligned Carbon Nanotube Arrays and Buckypapers by Dry Processes. *Carbon* **2010**, *48*, 868–875.
51. Mathur, A.; Roy, S. S.; Hazra, K. S.; Wadhwa, S.; Ray, S. C.; Mitra, S. K.; Misra, D. S.; McLaughlin, J. A. Oxygen Plasma Assisted End-Opening and Field Emission Enhancement in Vertically Aligned Multiwall Carbon Nanotubes. *Mater. Chem. Phys.* **2012**, *134*, 425–429.
52. Li, P.; Lim, X.; Zhu, Y.; Yu, T.; Ong, C.-K.; Shen, Z.; Wee, A. T.-S.; Sow, C.-H. Tailoring Wettability Change on Aligned and Patterned Carbon Nanotube Films for Selective Assembly. *J. Phys. Chem. B* **2007**, *111*, 1672–1678.
53. Dai, X.; Huang, X.; Yang, F.; Li, X.; Sightler, J.; Yang, Y.; Li, C. Enhanced Nucleate Boiling on Horizontal Hydrophobic-Hydrophilic Carbon Nanotube Coatings. *Appl. Phys. Lett.* **2013**, *102*, 1–5.
54. Li, H.; Geng, H.-Z.; Meng, Y.; Wang, Y.; Xu, X.-B.; Ding, E.-X.; Gao, J.; Chen, L.-T.; Ma, S. Fabrication and Test of Adhesion Enhanced Flexible Carbon Nanotube Transparent Conducting Films. *Appl. Surf. Sci.* **2014**, *313*, 220–226.
55. Chen, J.; Chen, Q.; Ma, Q. Influence of Surface Functionalization *via* Chemical Oxidation on the Properties of Carbon Nanotubes. *J. Colloid Interface Sci.* **2012**, *370*, 32–38.
56. Huang, J.-Q.; Zhang, Q.; Zhao, M.-Q.; Xu, G.-H.; Wei, F. Patterning of Hydrophobic Three-Dimensional Carbon Nanotube Architectures by a Pattern Transfer Approach. *Nanoscale* **2010**, *2*, 1401–1404.
57. Burton, Z.; Bhushan, B. Hydrophobicity, Adhesion, and Friction Properties of Nanopatterned Polymers and Scale Dependence for Micro- and Nanoelectromechanical Systems. *Nano Lett.* **2005**, *5*, 1607–1613.
58. Claussen, J. C.; Artiles, M. S.; McLamore, E. S.; Mohanty, S.; Shi, J.; Rickus, J. L.; Fisher, T. S.; Porterfield, D. M. Electrochemical Glutamate Biosensing with Nanocube and Nanosphere Augmented Single-Walled Carbon Nanotube Networks: A Comparative Study. *J. Mater. Chem.* **2011**, *21*, 11224–11231.
59. Shi, J.; Claussen, J. C.; McLamore, E. S.; Ul Haque, A.; Jaroch, D.; Diggs, A. R.; Calvo-Marzal, P.; Rickus, J. L.; Marshall Porterfield, D. A Comparative Study of Enzyme Immobilization Strategies for Multi-Walled Carbon Nanotube Glucose Biosensors. *Nanotechnology* **2011**, *22*, 1–10.
60. Skoog, D. A. Voltammetry. In *Principles of Instrumental Analysis*, 6th ed.; Thomson Brooks/Cole: Belmont, 2007; pp 737–742.

61. Liu, B.; Wang, M. Preparation and Characterization of Size-Controlled Silver Nanoparticles Decorated Multi-Walled Carbon Nanotubes and their Electrocatalytic Reduction Properties for Hydrogen Peroxide. *Russ. J. Electrochem.* **2014**, *50*, 476–481.
62. Yang, G.-W.; Gao, G.-Y.; Wang, C.; Xu, C.-L.; Li, H.-L. Controllable Deposition of Ag Nanoparticles on Carbon Nanotubes as a Catalyst for Hydrazine Oxidation. *Carbon* **2008**, *46*, 747–752.
63. Guo, D.-J.; Li, H.-L. High Dispersion and Electrocatalytic Properties of Palladium Nanoparticles on Single-Walled Carbon Nanotubes. *J. Colloid Interface Sci.* **2005**, *286*, 274–279.
64. Ovejero, G.; Sotelo, J. L.; Romero, M. D.; Rodríguez, A.; Ocaña, M. A.; Rodríguez, G.; García, J. Multiwalled Carbon Nanotubes for Liquid-Phase Oxidation. Functionalization, Characterization, and Catalytic Activity. *Ind. Eng. Chem. Res.* **2006**, *45*, 2206–2212.
65. Xin, Y.; Fujimoto, T.; Uyama, H. Facile Fabrication of Polycarbonate Monolith by Non-Solvent Induced Phase Separation Method. *Polymer* **2012**, *53*, 2847–2853.
66. Bazargan, A. M.; Keyanpour-rad, M.; Hesari, F. A.; Ganji, M. E. A Study on the Microfiltration Behavior of Self-Supporting Electrospun Nanofibrous Membrane in Water Using an Optical Particle Counter. *Desalination* **2011**, *265*, 148–152.
67. Kroll, S.; de Moura, M. O. C.; Meder, F.; Grathwohl, G.; Rezwan, K. High Virus Retention Mediated by Zirconia Microtubes with Tailored Porosity. *J. Eur. Ceram. Soc.* **2012**, *32*, 4111–4120.
68. Choudhary, V. R.; Gaikwad, A. G.; Sansare, S. D. Activation of Supported Pd Metal Catalysts for Selective Oxidation of Hydrogen to Hydrogen Peroxide. *Catal. Lett.* **2002**, *83*, 235–239.
69. Ishida, T.; Kuroda, K.; Kinoshita, N.; Minagawa, W.; Haruta, M. Direct Deposition of Gold Nanoparticles onto Polymer Beads and Glucose Oxidation with H_2O_2. *J. Colloid Interface Sci.* **2008**, *323*, 105–111.
70. Frikha, N.; Schaer, E.; Houzelot, J.-L. Experimental Study and Modelling of Thermal Runaway: Application to Dichromate Catalysed Hydrogen Peroxide Decomposition. *Thermochim. Acta* **2006**, *449*, 47–54.
71. Huang, H.-H.; Lu, M.-C.; Chen, J.-N. Catalytic Decomposition of Hydrogen Peroxide and 2-Chlorophenol with Iron Oxides. *Wat. Res.* **2001**, *35*, 2291–2299.
72. Seol, Y.; Javandel, I. Citric Acid-Modified Fenton's Reaction for the Oxidation of Chlorinated Ethylenes in Soil Solution Systems. *Chemosphere* **2008**, *72*, 537–42.
73. Mededovic, S.; Locke, B. Platinum Catalysed Decomposition of Hydrogen Peroxide in Aqueous-Phase Pulsed Corona Electrical Discharge. *Appl. Catal., B* **2006**, *67*, 149–159.
74. Hasnat, M. A.; Rahman, M. M.; Borhanuddin, S. M.; Siddiqua, A.; Bahadur, N. M.; Karim, M. R. Efficient Hydrogen Peroxide Decomposition on Bimetallic Pt−Pd Surfaces. *Catal. Commun.* **2010**, *12*, 286–291.
75. Pina, P.; Mallada, R. an Example of Falsified Kinetics by Diffusional Limitations in Gas-Solid Catalytic Reactions. *Int. J. Eng. Educ.* **2004**, *20*, 1074–1084.
76. McKee, D. W. Catalytic Decomposition of Hydrogen Peroxide by Metals and Alloys of the Platinum Group. *J. Catal.* **1969**, *14*, 355–364.
77. Wang, Z.; Lv, X.; Weng, J. High Peroxidase Catalytic Activity of Exfoliated Few-Layer Graphene. *Carbon* **2013**, *62*, 51–60.
78. Klaewkla, R.; Arend, M.; Hoelderich, W. F. A Review of Mass Transfer Controlling the Reaction Rate in Heterogeneous Catalytic Systems. In *Mass Transfer—Advanced Aspects*; Nakajima, H., Ed.; InTech: Rijeka, Croatia, 2011; pp 667−684.
79. Kopman, V.; Porfiri, M. Design, Modeling, and Characterization of a Miniature Robotic Fish for Research and Education in Biomimetics and Bioinspiration. *IEEE/ASME Trans. Mechatronics* **2013**, *18*, 471–483.
80. Aureli, M.; Kopman, V.; Porfiri, M. Free-Locomotion of Underwater Vehicles Actuated by Ionic Polymer Metal Composites. *IEEE/ASME Trans. Mechatronics* **2010**, *15*, 603–614.
81. Hubbard, J. J.; Fleming, M.; Palmre, V.; Pugal, D.; Kim, K. J.; Leang, K. K. Monolithic IPMC Fins for Propulsion and Maneuvering in Bioinspired Underwater Robotics. *IEEE J. Oceanic Eng.* **2014**, *39*, 540–551.
82. Zhengbao, Y.; Yukui, W.; Fei, G.; Zhenlong, W.; Yangwei, W. In *Study on the Hydrodynamics and Kinematics of a Biomimetic Fin Propulsor Actuated by SMA Wires*, Electronic and Mechanical Engineering and Information Technology (EMEIT), 2011 International Conference, **2011**.